PERGAMON

Acta mater. 48 (2000) 1055–1074

Acta MATERIALIA

www.elsevier.com/locate/actamat

ROLE OF INTERFACIAL AND MATRIX CREEP DURING THERMAL CYCLING OF CONTINUOUS FIBER REINFORCED METAL–MATRIX COMPOSITES

I. DUTTA

Center for Materials Science and Engineering, Department of Mechanical Engineering, Naval Postgraduate School, Monterey, CA 93943, USA

(Received 9 August 1999; accepted 21 October 1999)

Abstract—A uni-dimensional micro-mechanical model for thermal cycling of continuous fiber reinforced metal–matrix composites is developed. The model treats the fiber and matrix as thermo-elastic and thermo-elasto-plastic-creeping solids, respectively, and allows the operation of multiple matrix creep mechanisms at various stages of deformation through the use of unified creep laws. It also incorporates the effect of interfacial sliding by an interface-diffusion-controlled diffusional creep mechanism proposed earlier (Funn and Dutta, *Acta mater.*, 1999, **47**, 149). The results of thermal cycling simulations based on a graphite fiber reinforced pure aluminum matrix composite were compared with experimental data on a P100 graphite-6061 Al composite. The model successfully captured all the important features of the observed strain responses of the composite for different experimental conditions, such as the observed heating/cooling rate dependence, strain hysteresis, residual permanent strain at the end of a cycle, as well as both intrusion and protrusion of the fiber-ends relative to the matrix at the completion of cycling. The analysis showed that the dominant deformation mechanism operative in the matrix changes continually during thermal cycling due to continuous stress and temperature revision. Based on these results, a framework for the construction of a transient deformation mechanism map for thermal excursions of continuous fiber composites is proposed. *Published by Elsevier Science Ltd on behalf of Acta Metallurgica Inc.*

Keywords: Composites; Thermal cycling; Interfaces; Creep; Modeling

1. INTRODUCTION

Thermal cycling conditions are among the most severe environmental conditions for composites. The difference between the coefficients of thermal expansion of the matrix and the reinforcement causes large internal stresses to be induced in the composite during thermal cycling, often resulting in permanent dimensional changes and a pronounced strain hysteresis during cycling [1–10]. Furthermore, because of the continuous variation of the near-interface stress state during thermal cycling, substantial interfacial damage may potentially result [9–12].

A number of analytical treatments of thermal cycling in continuous fiber composites has been reported. Most of these have been based on one-dimensional models, where it is assumed that the interfaces are perfectly bonded and non-sliding, and that the fiber material undergoes thermo-elastic deformation only, whereas the matrix is subject to thermal, elastic, plastic, and sometimes, creep strains [5, 10, 12–16]. All these models predict extensive plastic flow of the matrix during cycling, which can include both rate-independent and rate-dependent plasticity. Because of this, the thermal cycling response often shows a dependence on heating and cooling rates, with slower rates resulting in greater permanent strains. The continuously varying stress and strain states within the composite during thermal cycling also causes the coefficient of thermal expansion of the composite to vary appreciably with temperature, thereby contributing to the strain hysteresis. Similar results have been obtained using a three-dimensional axisymmetric model [16], where it was also shown that the results from the three-dimensional model are qualitatively close to those obtained from one-dimensional models.

Although the micro-mechanical details of the stress and strain excursions during thermal cycling are reasonably well understood, the role of the interface is still a subject of significant confusion. Continuous fiber reinforced composites are generally thought to deform with the matrix and fiber in isostrain condition. However, there is ample evidence in the literature that this condition is often violated, even in the absence of interfacial fracture. This is most clearly observed following thermal

1359-6454/00/$20.00 Published by Elsevier Science Ltd on behalf of Acta Metallurgica Inc.
PII: S1359-6454(99)00402-4

cycling of composites in the absence of any applied load [10, 11]. For instance, Yoda *et al.* [11] observed that the ends of W fibers in a Cu matrix intruded into the matrix following thermal cycling, the extent of intrusion increasing with increasing number of cycles. Similar effects have been observed following *slow* thermal cycling of graphite fiber reinforced aluminum composites [10], whereupon the matrix was observed to protrude past the fiber-ends. In both cases [10, 11], the slow heating/cooling rates during cycling, in conjunction with the tensile matrix residual stress along the fiber axes, allowed the matrix to *elongate* relative to the fibers via creep. Here, no interfacial debonding occurs, and the differential strain between the matrix and fibers is accommodated by *time-dependent diffusional sliding* at the interface close to the fiber-ends, where large interfacial shear stresses exist. This is very different from the effect observed during relatively *rapid* thermal cycling, where interfacial fracture, followed by *frictional sliding* at the debonded interface, results in the relief of axial tensile residual stresses in the matrix, allowing the matrix to *shrink* relative to the fibers [9, 17]. Frictional sliding is commonly observed in composites with weak interfaces which undergo debonding during cycling [9, 12, 17], whereas time-dependent sliding via interfacial creep occurs in the absence of debonding [10, 11].

So far, most models (e.g. Ref. [12]) have treated interfacial sliding either as a frictionally controlled process (debonded interface) or as a shear flow process (bonded interface). However, such approaches do not account for sliding due to creep processes (akin to grain boundary sliding) which are likely to be prevalent at elevated temperatures, even in the absence of debonding or matrix plastic flow.

Based on experimental observations of the creep behavior of bulk composites, the interfacial contribution to creep has been thought of in several different ways. First, the interface has been thought to be a highly dislocated region, wherein diffusionally accommodated recovery processes may lead to relative translation between the matrix and reinforcement [18–20]. This type of behavior may be represented by a power-law creeping interfacial region, which has been the basis for a number of composite creep models proposed in the literature (e.g. Refs [18, 20–22]). Alternatively, the accommodation of differential matrix and fiber strains has been thought to occur by a mechanism coupling diffusive transport and viscous drag along the interface [23–25], where both phenomena have linear stress dependence.

Recently, the creep behavior of well-bonded interfaces was experimentally isolated and studied for the first time [26] by utilizing model single fiber composites in conjunction with a fiber push-down approach, whereby the interface was loaded in shear. The interface was found to slide via interface-diffusion-controlled diffusional creep with a threshold stress (Bingham flow), with the interface acting as a high diffusivity path. Analytical modeling based on the approach of Raj and Ashby [27] produced an explicit constitutive law for interfacial sliding in the absence of interfacial fracture, and revealed that the observed threshold stress was directly related to the normal (radial) stress acting on the fiber matrix interface [26]. In subsequent work [28], matrix and fiber strains in specially designed samples of a model single fiber composite were separately measured during isothermal tensile creep experiments in order to detect the effect of interfacial sliding. The fiber and matrix were found to strain differentially along the fiber axial direction, with interfacial sliding being confined to the regions near free surfaces at the extremities of the gauge length, where large interfacial shear stresses were present. A uni-dimensional micro-mechanical model for composite creep, incorporating the interfacial creep law proposed in Ref. [26], was developed, and it was found that the model closely simulated the experimentally observed differential strain response of the matrix and the fiber, and therefore, the role of interfacial sliding during isothermal creep. From a practical standpoint, interfacial sliding becomes important during tensile creep only in the absence of end-constraints on the specimen (e.g. in turbine blades), or when the ratio of the specimen gauge length to the fiber diameter (L/d_f) is small enough for interfacial shear stresses to be significant within the gauge section [28]. Under such circumstances, the composite creep rate can be finite even after long times at a constant applied stress, whereas in the absence of interfacial sliding, the creep rate would eventually vanish with time [28]. Under thermal cycling conditions, end constraints such as those imposed on the grip sections of a tensile creep sample are usually absent, and interfacial shear stresses are continually generated and relieved at the extremities of the sample. Thus the effects of interfacial creep are expected to be substantially more prominent during thermal cycling.

In addition to fostering interfacial creep, thermal cycling conditions can also produce changes in the dominant operative matrix creep mechanism commensurate with the continuous changes in temperature and matrix stress. Although most studies of creep and thermal cycling of composites reported to date consider only one dominant matrix creep mechanism (e.g. Refs [5, 10, 11, 14, 18–20]), it has been recognized that unified creep laws are necessary to adequately describe the composite strain response when the temperature and matrix stress vary considerably, as during thermal cycling [29]. The role of mechanism transitions has been investigated in metal ceramic multi-layers, where the dominant creep mechanism of the metallic layer(s) has been found to change continually during thermal cycling [30]. However, the impact of creep mechanism tran-

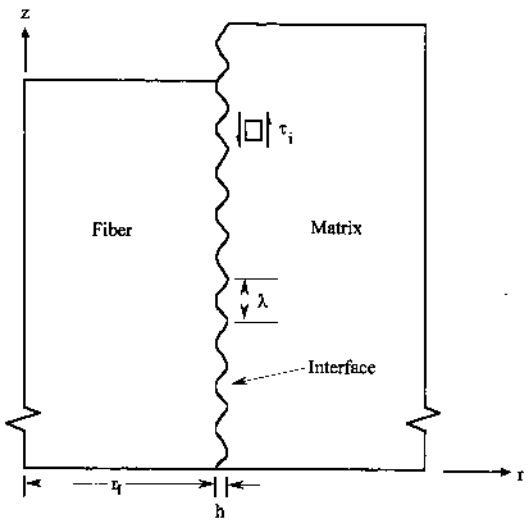

Fig. 1. Schematic of the fiber/matrix interfacial region used in modeling, showing a periodic interfacial topography with a width h and a periodicity λ. The axial coordinate z is zero at the middle of the fiber length and the radial coordinate r is zero at the middle of the fiber diameter.

sitions during thermal cycling of fibrous composites has not been addressed yet.

The purpose of this paper is therefore twofold: (1) to model the thermal cycling response of continuous fiber metallic composites, incorporating the effects of interfacial sliding and the operation of multiple matrix creep mechanisms, with the aim of understanding the role/importance of diffusion controlled interfacial sliding and matrix creep mechanism transitions; and (2) to compare the analytical results with experiments based on continuous graphite fiber reinforced aluminum composites in order to assess the applicability of the model, in particular with respect to interfacial sliding during thermal cycling.

2. APPROACH

2.1. Analytical

A one-dimensional model for the axial strain response of continuous fiber composites during axial creep, accounting for interfacial creep due to the presence of interfacial shear stresses near the ends of the fiber, is developed here. The general approach is identical to that utilized in earlier work to model isothermal creep [28]. It is assumed that the fiber and the matrix are thermo-elastic and thermo-elasto-plastic-creeping solids, respectively. The model accounts for interfacial sliding via diffusionally accommodated mechanisms [26], as well as possible changes in the matrix creep mechanisms during thermo-mechanical excursions, which have been incorporated by utilizing unified steady state dislocation and diffusional creep laws [31].

A schematic of the interfacial region, as conceptualized for the model, is shown in Fig. 1, which depicts half the axial length of the composite, with the axial coordinate z being zero at the middle of the fiber length, and the radial coordinate r being zero at the middle of the fiber diameter. During thermal cycling, a shear stress τ_i, which varies with the axial coordinate z, is generated at the interface. τ_i is zero at $z = 0$, and maximum at the fiber-ends ($z = l_f/2$). As in Refs [26, 28], the interface is assumed to be microscopically periodic with a width of h and a periodicity of λ.

Based on the constitutive law developed in Ref. [26], the strain rate due to interfacial sliding can be represented as

$$\dot{\gamma}_i = A_i(\tau_i - \tau_0) \tag{1}$$

where τ_i is the shear stress acting on the interface, τ_0 is a threshold shear stress, and

$$A_i = \frac{4\delta_i D_{i_0}\Omega}{kTh^3}\exp\left[-\frac{Q_i}{RT}\right] \tag{2}$$

where Q_i and D_{i_0} are the activation energy and frequency factor, respectively, for interfacial diffusion, k is Boltzmann's constant, R is the gas constant, T is the absolute temperature, Ω is the atomic volume of the diffusing species (matrix), and δ_i is the thickness of the interface. Following Ref. [26], the threshold stress τ_0 is expressed as

$$\tau_0 = 2\pi^3\left(\frac{h}{\lambda}\right)^3\sigma_R \tag{3}$$

where σ_R is the radial compressive stress acting on the interface due to the coefficient of thermal expansion and/or Poisson's ratio mismatch between the matrix and fiber.

The overall solution scheme for predicting the strain responses of the fiber and the matrix separately is outlined below. Additional details of the analysis are available in Ref. [28]. When the matrix and fiber are in a non-isostrain state, stress equilibrium under a constant applied stress σ_c requires that

$$\sigma_c = \sigma_m V_m + \sigma_f V_f\left[\frac{1+\bar{\varepsilon}_m}{1+\bar{\varepsilon}_f}\right] \tag{4}$$

where σ_m is the axial matrix stress, σ_f is the axial fiber stress, V_m and V_f are the volume fractions of the matrix and fiber, respectively, and $\bar{\varepsilon}_m$ and $\bar{\varepsilon}_f$ are the average axial strains of the matrix and fiber, respectively. Strain continuity across the interface requires that

$$\frac{l_0}{2}(\bar{\varepsilon}_m - \bar{\varepsilon}_f) = h\gamma_i \tag{5}$$

where l_0 is the nominal gauge length (shorter of the matrix or fiber lengths), $\bar{\varepsilon}_m$ and $\bar{\varepsilon}_f$ represent average

strain values over half the gauge length ($z = 0$ to $l_0/2$), γ_i is the interfacial shear strain at $z = l_0/2$, and is given by [see equation (1)]

$$\gamma_i = \dot{\gamma}_i t = A_i[\tau_i(z = l_0/2) - \tau_0]t. \tag{6}$$

The matrix and fiber strains $\bar{\varepsilon}_m$ and $\bar{\varepsilon}_f$ are given by

$$\bar{\varepsilon}_m = \bar{\varepsilon}_m^{th} + \bar{\varepsilon}_m^{el} + \bar{\varepsilon}_m^{pl} + \bar{\varepsilon}_m^{cr} \tag{7}$$

and

$$\bar{\varepsilon}_f = \bar{\varepsilon}_m^{th} + \bar{\varepsilon}_f^{el} \tag{8}$$

where the superscripts th, el, pl and cr represent the thermal, elastic, plastic and creep components. The expressions for the individual strain components on the right-hand side of equations (7) and (8) are given in the Appendix.

Rewriting equation (5) in incremental form and substituting for $\Delta\bar{\varepsilon}_m$, $\Delta\bar{\varepsilon}_f$ and $\Delta\gamma_i$ using equations (4) and (6), and equations (A1)–(A6) (Appendix) yields

$$\alpha_m\Delta T + \frac{\Delta\sigma_m}{E_m} + \frac{\Delta\sigma_m}{RWH} + \Delta\varepsilon_m^{cr} - \left[\alpha_f\Delta T + \frac{\Delta\sigma_c - \Delta\sigma_m V_m}{E_f V_f}\left(\frac{1+\bar{\varepsilon}_m}{1+\bar{\varepsilon}_f}\right)\right] = \frac{2h}{l_0}A_i\Delta t\left[\tau_i\left(z = \frac{l_0}{2}\right) - \tau_0\right]. \tag{9}$$

From above, the incremental change in the matrix stress is

$$\Delta\sigma_m = -\left[\frac{\Delta\alpha\Delta T + \Delta\varepsilon_m^{cr} - \frac{\Delta\sigma_c}{E_f V_f}\left(\frac{1+\bar{\varepsilon}_m}{1+\bar{\varepsilon}_f}\right) - \frac{2h}{l_0}A_i\Delta t\left[\tau_i\left(z = \frac{l_0}{2}\right) - \tau_0\right]}{\frac{V_m}{E_f V_f}\left(\frac{1+\bar{\varepsilon}_m}{1+\bar{\varepsilon}_f}\right) + \frac{1}{E_m} + \frac{1}{RWH}}\right] \tag{10}$$

where RWH is rate of work hardening of the matrix, given by

$$RWH = \frac{d\sigma_m}{d\varepsilon_m^{pl}} = K_1 n_1\left[\frac{\sigma_m - \sigma_m^{ys}}{K_1}\right]^{(n_1-1)/n_1}$$

K_1 and n_1 being the matrix work hardening coefficient and exponent, respectively, and $\tau_i(z = l_0/2)$ represents the interfacial shear stress at $z = l_0/2$ at the beginning of the solution step.

The interfacial shear stress τ_i can be calculated as a function of z by using a modified shear-lag approach after incorporating the effects of matrix plasticity and creep, and is given by [28]

$$\tau_i = \frac{r_f}{2}B_1\sqrt{\frac{H_1}{E_f}}\sinh\left(z\sqrt{\frac{H_1}{E_f}}\right) \quad \text{for } z < z_0 \tag{11}$$

and

$$\tau_i = A_0 + (\tau_m^{ys} - A_0)\left(\frac{z}{z_0}\right)^{1/B_0} \quad \text{for } z \geq z_0 \tag{12}$$

where z_0 is the value of z beyond which the matrix at the interface undergoes yielding in shear, given by

$$z_0 = \frac{1}{\beta}\sinh^{-1}\left(\frac{2\tau_m^{ys}}{r_f B_1 \beta}\right) \tag{13}$$

where r_f is the fiber radius, E_f is the Young's modulus of the fiber, and τ_m^{ys} is the temperature-dependent shear yield strength of the matrix. The parameters H_1, B_1, A_0 and B_0 in equations (11) and (12) are given by equations (14)–(17) below [28]:

$$H_1 = \frac{2}{r_f[N + M + Q_2]} \tag{14}$$

$$B_1 = \frac{-E_f\bar{\varepsilon}_m}{\cosh\left(\frac{\beta l_0}{2}\right)} \tag{15}$$

$$A_0 = \tau_m^{ys}\left(1 - \frac{K''}{G_m}\right) \tag{16}$$

$$B_0 = \frac{K''}{h}(N' + M + Q_2) \tag{17}$$

where $N = r_f(1/G_m + A'')\ln(R/r_f)$, $M = hA_i t$, $Q_2 = (Anr_f^n/(1-n))(R^{1-n} - r_f^{1-n})\tau_i^{n-1}$, $N' = r_f(1/G_m + 1/K'' + A'')\ln(R/r_f)$, $R = r_f/\sqrt{V_f}$, $\beta = \sqrt{H_1/V_f}$, and G_m is the shear modulus of the matrix, $A = A_{disl} \cdot t$ and $A'' = A_{diff} \cdot t$ [A_{disl} and A_{diff} being the matrix creep coefficients for power-law dislocation and diffusional creep, respectively (Appendix)], n is the stress exponent for power-law matrix creep, and K'' is the linear work hardening coefficient of the matrix in shear.

The threshold shear stress for interfacial creep, τ_0, can be obtained using equation (3) based on the temperature-dependent value of the interfacial nor-

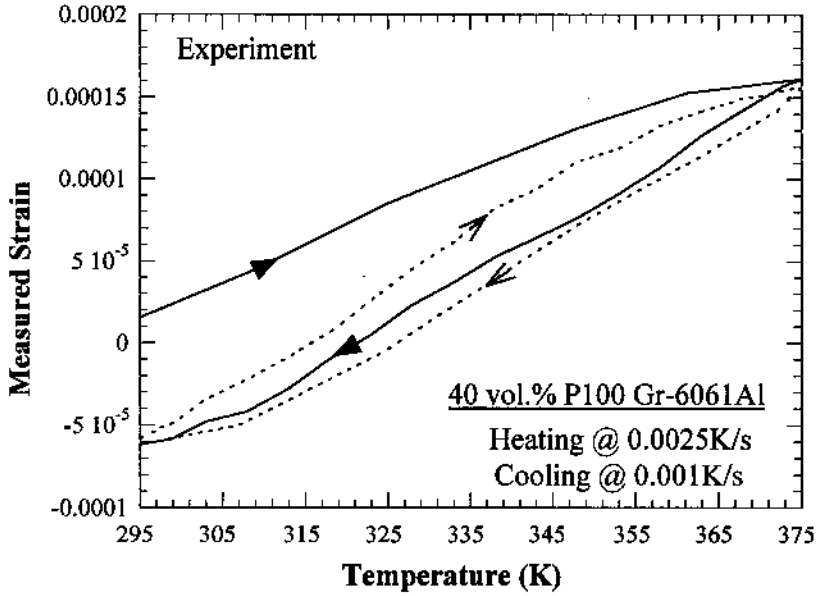

Fig. 2. Experimental axial strain response of a P100 graphite fiber reinforced 6061 Al composite during two thermal cycles over a temperature range of 293–373 K (1st cycle = solid arrows; 2nd cycle = line arrows).

mal (radial) stress σ_R. For an aluminum–matrix composite, σ_R may be assumed to be zero at 800 K, rising to a value of σ_{R_0} at 300 K in inverse proportionality with temperature, yielding (after Ref. [28])

$$\sigma_R = \sigma_{R_0}\left[\frac{480}{T} - 0.6\right]. \tag{18}$$

During heating/cooling in the absence of an applied stress, and/or during isothermal creep at a constant stress, $\Delta\sigma_c = 0$. Hence the incremental change in the matrix stress [equation (10)] becomes

$$\Delta\sigma_m = -\left[\frac{\Delta\alpha\Delta T + \Delta\varepsilon_{in}^{cr} - \dfrac{2h}{l_0}A_i\Delta t\left[\tau_i\left(z=\dfrac{l_0}{2}\right)-\tau_0\right]}{\dfrac{V_m}{E_f V_f}\left(\dfrac{1+\bar{\varepsilon}_m}{1+\bar{\varepsilon}_f}\right)+\dfrac{1}{E_m}+\dfrac{1}{RWH}}\right] \tag{19}$$

where $\tau_i(z = l_0/2)$ can be calculated from equations (11) or (12).

The basic solution procedure to obtain the stress/strain state of the matrix/fiber during a thermo-mechanical excursion consists of: (1) calculating the initial matrix stress state σ_{m_0} at the start of the thermo-mechanical excursion; (2) calculating the incremental stress change $\Delta\sigma_m$ using equation (19); (3) updating the matrix stress as $\sigma_{m_j} = \sigma_{m_{j-1}} + \Delta\sigma_m$ (here the subscript j represents the jth solution step); and then (4) computing the matrix and fiber strain components using equations (A1)–(A6). This procedure is utilized iteratively, allowing the temperature and/or time to change incrementally. At each solution step, the stress and strain increments are calculated and the matrix and fiber stress/strain are updated. This was achieved using a computer program written in the MATLAB® programming language.

2.2. Experimental

Thermal cycling experiments were conducted on a unidirectionally reinforced, cast 40 vol.% P100 Thornel graphite fiber reinforced 6061 Al composite obtained from Fiber Materials Inc., Columbus, Ohio, using rectangular bar specimens (25.4 × 5.5 × 3 mm^3) with the specimen length aligned along the fiber axes. The longitudinal thermal strain response of the composite was measured at various heating/cooling rates using an Orton® automatic recording dilatometer between a lower limit of 293 K and an upper limit of either 603 K or 373 K. The heating and cooling rates used in all the experiments fell within the *slow* cycling regime, so as to foster creep conditions at the interface and within the matrix, and preclude interfacial fracture/debonding. All testing was conducted in argon atmosphere.

To observe the effect of interfacial sliding during thermal cycling, 10 × 10 mm^2 billets were cycled in the dilatometer, but without the sample contacting the push-rods. Periodically, cycling was interrupted and the samples were inspected under the scanning electron microscope (SEM). Additionally, transmission electron microscopy (TEM) was used to observe the interfacial region before and after thermal

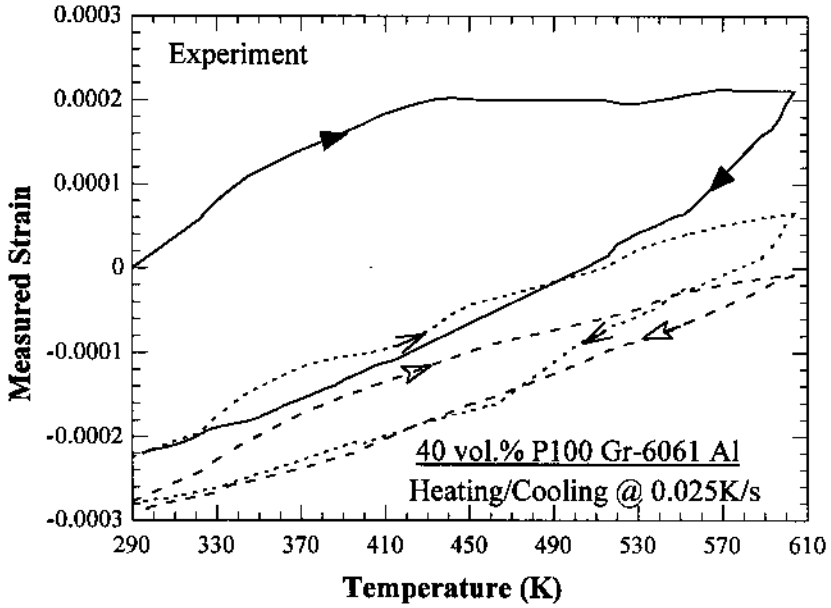

Fig. 3. Experimental axial strain response of a P100 graphite fiber reinforced 6061 Al composite during three thermal cycles over a temperature range of 293–603 K (1st cycle = solid arrows; 2nd cycle = line arrows; 3rd cycle = open arrows).

excursions on samples prepared by standard techniques (e.g. Ref. [10]).

3. RESULTS

3.1. Experimental

Figures 2 and 3 show the measured longitudinal strain response of the P100 graphite–6061 Al matrix composite during two thermal cycles between 293 and 373 K, and three thermal cycles between 293 and 603 K, respectively. Consistent with previous reports, a substantial strain hysteresis and a distinct knee in the heating curve are observed in both cases, these effects being more prominent during the first cycle. Comparing the strain response during the first cycle in the two figures, it is apparent that the knee occurs at a lower temperature (~360 K) in Fig. 2, where the heating rate is 0.0025 K/s, than in Fig. 3 (~430 K), where the heating rate is 0.025 K/s. Clearly, the thermal cycling response of the composite is strongly rate dependent. Also apparent in both figures is a compressive residual permanent strain at the end of the first cycle, indicating that the composite length is shorter following the first cycle than at the start. During subsequent cycling, the residual strain decreases, and eventually vanishes (after two cycles for 293–373 K and three cycles for 293–603 K), although the strain hysteresis remains.

Figures 4 and 5 show the extremities of two composite samples viewed end-on in the SEM following cycling up to 373 and 603 K, respectively. Prior to the experiments, the sample surfaces were ground to a 1 μm finish in order to ensure that the fiber-ends were flush with the matrix. It is apparent that after three cycles till 373 K, the matrix protrudes slightly beyond the fiber-ends. Contrarily, after three cycles till 603 K, the fiber-ends are observed to protrude significantly beyond the matrix. Clearly, in neither case are the matrix and fiber in isostrain condition. Interestingly, there appears to be no evidence of interfacial fracture [which is typically manifested in the form of a crevice around the fiber perimeter (e.g. Ref. [9])] in either case. Energy dispersive X-ray analysis of the cylindrical surfaces of the protruding fibers revealed the presence of Al, Mg and O. This is consistent with the structure of the interfacial region, as observed in the bright field TEM micrograph in Fig. 6, where a 0.3–0.4 μm thick inter-phase of spinel ($MgAl_2O_4$) is seen to be present between the Al matrix and the graphite fiber. In the absence of interfacial fracture, it may be presumed that the differential strain arises due to diffusionally accommodated sliding at the spinel–Al interface during the thermal cycling experiments.

3.2. Analytical

The approach outlined in Section 2.1 was utilized to model the fiber and matrix strain responses

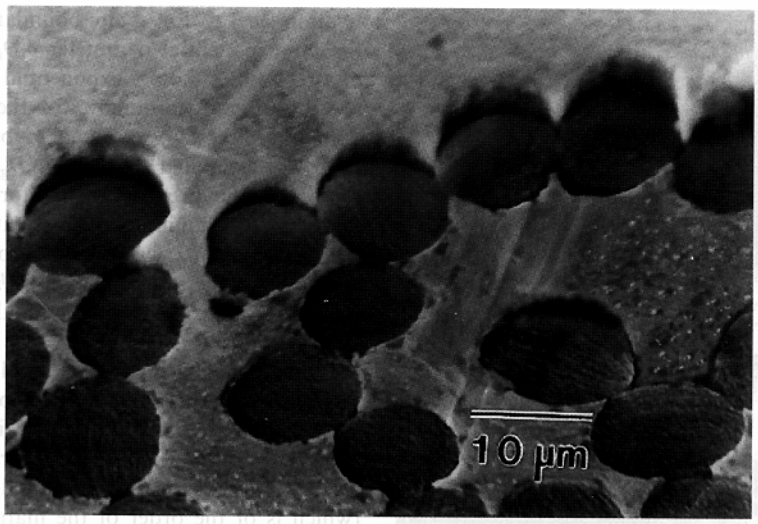

Fig. 4. SEM image of the surface of the experimental composite following three cycles from 293 to 373 K at heating and cooling rates of 0.0025 and 0.001 K/s, respectively, showing some of the fiber-ends intruding into the matrix.

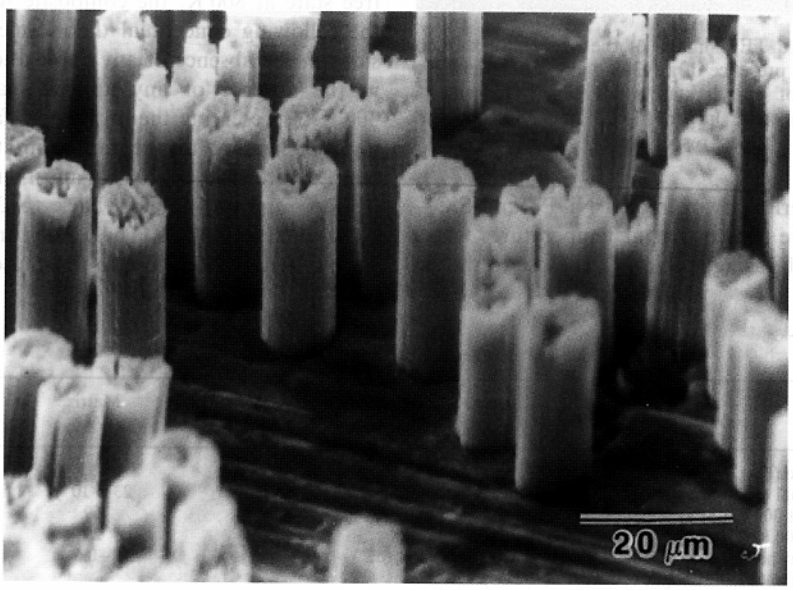

Fig. 5. SEM image of the surface of the experimental composite following three cycles from 293 to 603 K at heating and cooling rates of 0.025 K/s, showing the fibers protruding significantly from the matrix. There is no evidence of interfacial fracture.

during thermal cycling (in the absence of applied load) of a commercially pure aluminum–matrix composite reinforced with 40 vol.% of P100 graphite fibers†. Table 1 lists the relevant data used in the model. The properties of the elastic fiber (graphite is entirely elastic and non-creeping within the stress and temperature conditions of the present experiments) were obtained from Ref. [33], those of the elasto-plastic matrix were obtained from Ref. [34], whereas the other data relevant to the creep behavior of pure Al matrix were obtained from Ref. [31].

Since experimental data on the creep behavior of graphite–aluminum interfaces are not available, the data used to represent the creep properties of the interface were inferred on the basis of the results reported in Ref. [26]. The five unknown parameters in the interfacial sliding rate equation [equation (1), along with equations (2) and (3)] are σ_R, Q_i, h/λ, h

† For modeling, a pure aluminum matrix was chosen (rather than a 6061 Al matrix) because of the ready availability of comprehensive materials data required for consideration of creep mechanism transitions through the use of unified creep laws [31].

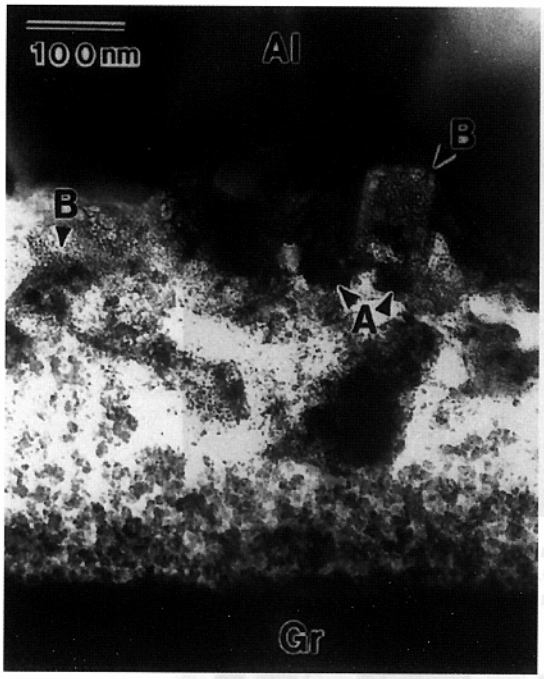

Fig. 6. Bright field TEM image of the fiber–matrix interface, showing the presence of a 0.3–0.4 μm wide interfacial zone consisting of fine crystallites of $MgAl_2O_4$, with A and B indicating some larger Al-rich and Mg-rich particles, respectively.

and $\delta_i D_{i_0}$. Experiments on model Ni–Pb and SiO_2–Pb systems have shown that at temperatures where only Pb is the diffusing species, Q_i is close to the activation energy for grain boundary diffusion, and the pre-exponential parameter $\delta_i D_{i_0}$ is on the order of 10–50 times the pre-exponential for grain boundary diffusion. Accordingly, for the graphite–aluminum interface, Q_i was taken to be 84 kJ/mol, and $\delta_i D_{i_0}$ was estimated to be $10\delta_{gb}D_{gb_0}$, where $\delta_{gb}D_{gb_0}$ represents the pre-exponential for grain boundary diffusion in aluminum. Consistent with Ref. [26], the parameter h/λ was assumed to have a value of 0.1, whereas the interfacial width h was taken to be 0.1 μm. Finally, the radial residual stress acting on the interface at 298 K (σ_{R_0}) was estimated to be 15 MPa (~a quarter of the axial matrix stress at 298 K). This was based on experimental results from the literature [35], which indicate that the transverse residual stresses in graphite–aluminum are substantially smaller than the longitudinal stress (which is of the order of the matrix yield strength) because of the relatively small difference between the transverse modulus of pitch fibers ($\sim 20 \times 10^{-6}$/K) and aluminum (24×10^{-6}/K).

Assuming the matrix to be in an initially stress-free state at 800 K, the composite was subjected to the following conceptual thermo-mechanical excursions in the absence of any applied load: (1) cooling in the absence of any applied load at 1 K/s to 300 K, representing the initial post-fabrication cooling; (2) heating to the maximum thermal cycling temperature (380 or 600 K) at either 0.001, 0.05 or 0.5 K/s; and (3) cooling back to 300 K at either 0.001, 0.05 or 0.5 K/s. These rates and temperatures were selected to be close to those used in the exper-

Table 1. Properties and constants used in calculation

		Matrix Al	Fiber Graphite
Melting temperature (K)		933	N/A
Coefficient of thermal expansion (/K)		23×10^{-6}	-1×10^{-6}
Young's modulus at 300 K (GPa)		69	690
Shear modulus at 300 K (GPa)		25	
Temperature dependence for modulus calculations, $\Delta=(T_m/G_m)(dG_m/dT)$		−0.5	
Temperature-dependent yield strength of matrix (1100 Al):			
$T \leq 533$ K: $\sigma_{ys}=PP+QQ \times T+RR \times T^2$ (MPa)	PP	22.6235	
	QQ	0.1049	
	RR	−0.0002	
$T \geq 533$ K: $\sigma_{ys}=MM \exp(NN \times T)$ (MPa)	MM	195.38	
	NN	−0.0045	
Temperature-dependent Young's modulus		$E_m = E_{m0}(1+\Delta(T-300)/T_m)$	
Temperature-dependent shear modulus		$G_m = G_{m0}(1+\Delta(T-300)/T_m)$	
Temperature-dependent work hardening coefficient		$K_1 = K_{1_0}(1+\Delta(T-300)/T_m)$	
Work hardening coefficient at 300 K, K_{1_0} (MPa)		700	
Work hardening exponent, n_1		0.5	
Frequency factor for lattice diffusion, D_{l_0} (m^2/s)		1.7×10^{-4}	
Activation energy for lattice diffusion, Q_l (J/mol)		142,000	
Pre-exp. for grain bdy diffusion, $\delta_{gb}D_{gb_0}$ (m^3/s)		5.0×10^{-14}	
Activation energy for grain bdy diffusion, Q_{gb} (J/mol)		84,000	
Pre-exponential for pipe diffusion, $a_p D_{p_0}$ (m^4/s)		7×10^{-25}	
Activation energy for pipe diffusion, Q_p (J/mol)		82,000	
Burgers vector, b (m)		2.86×10^{-10}	
Atomic volume, Ω (m^3)		1.66×10^{-29}	
Dorn constant, A		3.4×10^6	
Dislocation creep exponent, n		4.4	
Power-law breakdown parameter, α'		1000	
Matrix grain size, d (m)		25×10^{-6}	
Fiber radius, r_f (m)		–	5×10^{-6}

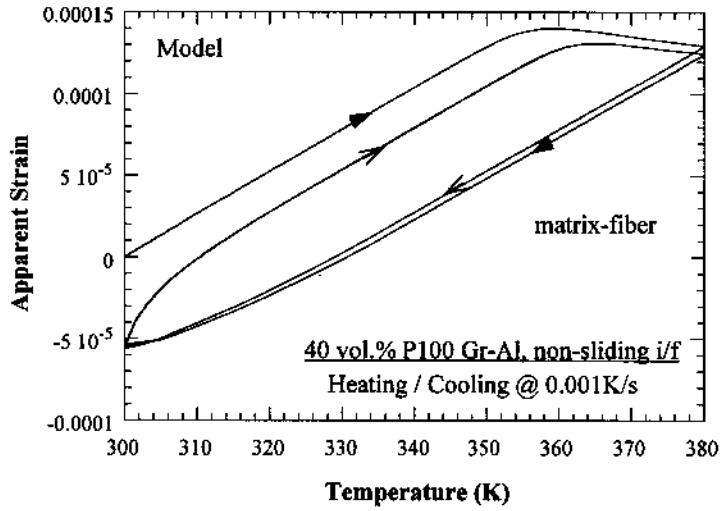

Fig. 7. Computed axial strain response of the composite for two cycles between 300 and 380 K in the absence of interfacial sliding (1st cycle = solid arrows; 2nd cycle = line arrows).

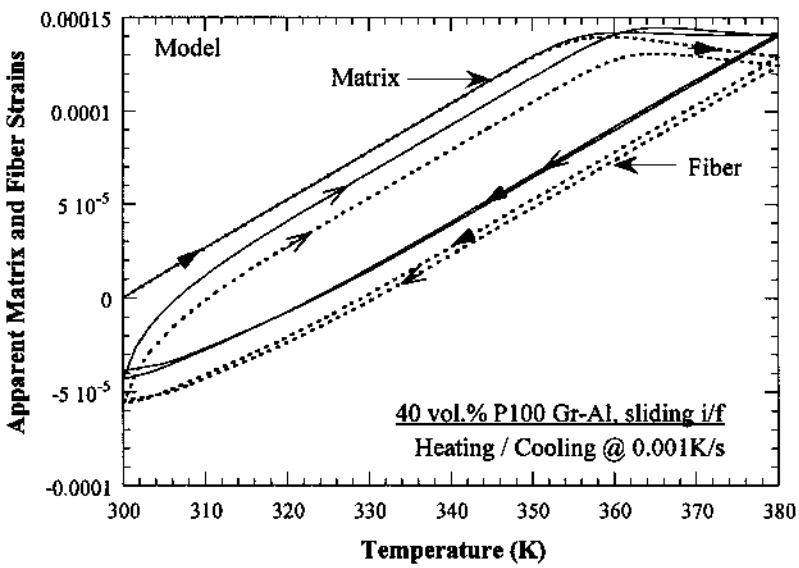

Fig. 8. Computed axial strain response of the composite for two cycles between 300 and 380 K in the presence of interfacial sliding, showing divergence between matrix and fiber strains. The final fiber length is less than that of the matrix (1st cycle = solid arrows; 2nd cycle = line arrows).

iments. During each step, the internal axial stress and strain states in the constituents are computed as a function of temperature/time, in order to model the overall behavior of the composite during thermal cycling†. It is worth noting here that our model utilizes only steady state equations for creep, and therefore, the computed instantaneous creep rates are expected to deviate somewhat from the actual material response, especially at the higher temperatures [30].

Figures 7 and 8 show a plot of the computed axial composite strain during two thermal cycles from 300 to 380 K, in the absence of, and in the presence of interfacial sliding, respectively. In both

† The one-dimensional model ignores the contribution of transverse stresses, except in the interfacial creep equation, where an estimate of the radial residual stress σ_R is utilized for determining the threshold stress.

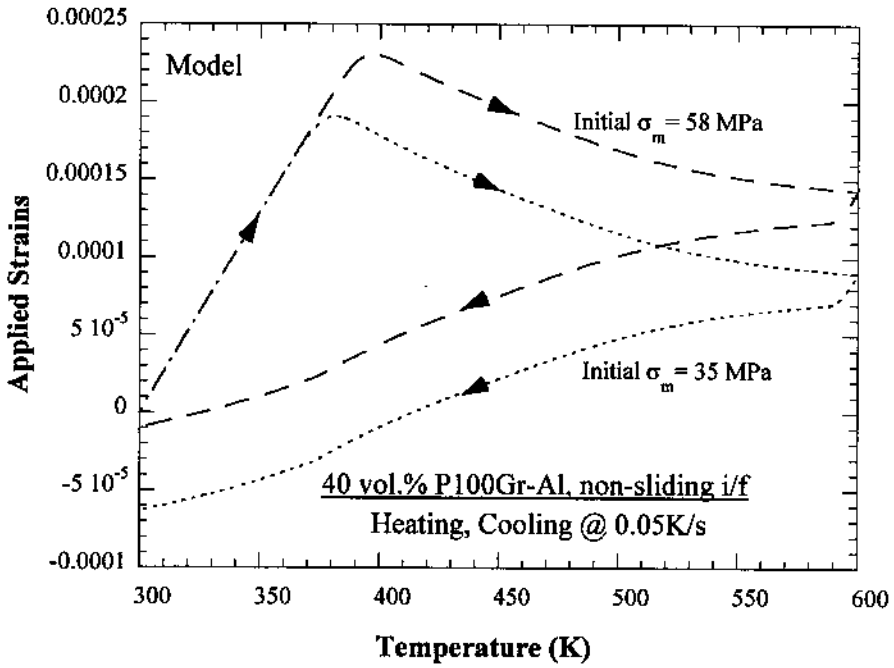

Fig. 9. Computed axial strain response of the composite for one cycle between 300 and 600 K in the absence of interfacial sliding for two different initial matrix stress (σ_{m_0}) levels. The permanent strain at the end of the cycle increases with decreasing σ_{m_0}.

cases, the heating and cooling rates are 0.001 K/s. The overall strain responses are observed to be very similar, except that in the absence of interfacial sliding, the fiber and matrix are in isostrain condition, whereas in the presence of sliding, they strain differently. Figures 7 and 8 also agree reasonably well with the experimental results (Fig. 2). Consistent with the experiments, a strain hysteresis and a distinct knee in the heating curve are observed. Also observed is a compressive residual permanent strain at the end of the first cycle, which disappears at the end of the second cycle. The origins of these will be discussed later. Of particular interest is the observation that under the conditions of the present simulation, the final length of the fiber is less than that of the matrix (i.e. the fiber *intrudes* into the matrix) in the presence of interfacial sliding (Fig. 8). It is apparent that most of this differential deformation (which causes the length difference) occurs during the first cycle.

Figure 9 plots the strain response when the composite is once cycled between 300 and 600 K at 0.05 K/s in the absence of interfacial sliding, for a starting matrix stress (σ_{m_0}) of 58 or 35 MPa. Following initial cooling from the fabrication temperature (from 800 to 300 K at 1 K/s), the axial matrix stress present in the work-hardened matrix is 58 MPa (the same as the new yield strength). With time, some of this stress is likely to be relieved due to recovery processes operative at ambient temperature in the pure Al matrix. Therefore, the effects of two different σ_{m_0} levels are considered. It is observed that commensurate with a decrease of the initial stress σ_{m_0} from 58 to 35 MPa, the residual permanent strain at the end of the cycle increases significantly. The rationale for this will be discussed subsequently.

Figure 10 shows the computed composite strain response during three thermal cycles from 300 to 600 K at 0.05 K/s in the presence of interfacial sliding. In addition to the hysteresis, knee and the residual permanent strain (as observed in Fig. 9), it is seen that under these conditions, the fiber length is greater than that of the matrix (i.e. the fiber *protrudes* out of the matrix) at the end of the first cycle. The difference between the matrix and fiber lengths increases slightly during subsequent cycling, the rate of increase decreasing and eventually vanishing with increasing number of cycles, as observed experimentally. This protrusion of fibers relative to the matrix is in contrast to the fiber intrusion that was observed at the end of the 300–380 K cycle. It is thus apparent that a diffusionally accommodated interfacial creep mechanism can rationalize both fiber intrusions as well as fiber protrusions during thermal cycling.

Comparing the cooling segment of the first cycle in Fig. 10 (analytical) with that in Fig. 3 (experimental), it is observed that the experimental curve is convex down, whereas the analytical fiber strain trace is concave down. Since the fiber protrudes out of the matrix, it may be expected that the exper-

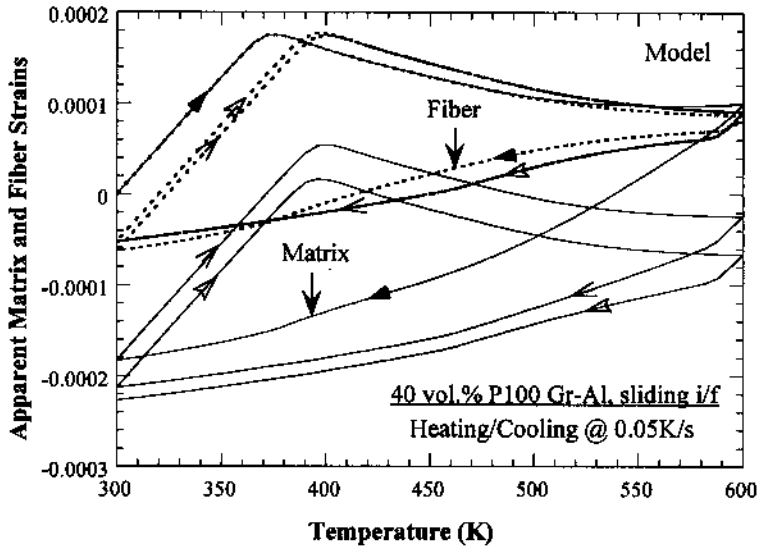

Fig. 10. Computed axial strain response of the composite for three cycles between 300 and 600 K in the presence of interfacial sliding. The final fiber length is significantly greater than that of the matrix (1st cycle = solid arrows; 2nd cycle = line arrows; 3rd cycle = open arrows).

imental dilatometer trace should follow the fiber dimensions. This apparent discrepancy may be rationalized by realizing that the ends of the dilatometry specimens were bevelled and rounded to minimize their contact areas with the push-rods, thereby allowing the protruding fibers to perhaps bend away from the push-rods, which then essentially track the matrix displacement (which is convex downward, as seen in Fig. 10). In fact, the ends of the fibers protruding from the matrix at and near the region of contact with the push-rods were frequently observed to be damaged or broken, supporting the above inference.

We now rationalize the matrix and fiber strain responses noted in Fig. 10 on the basis of the variation of the individual stress and strain components

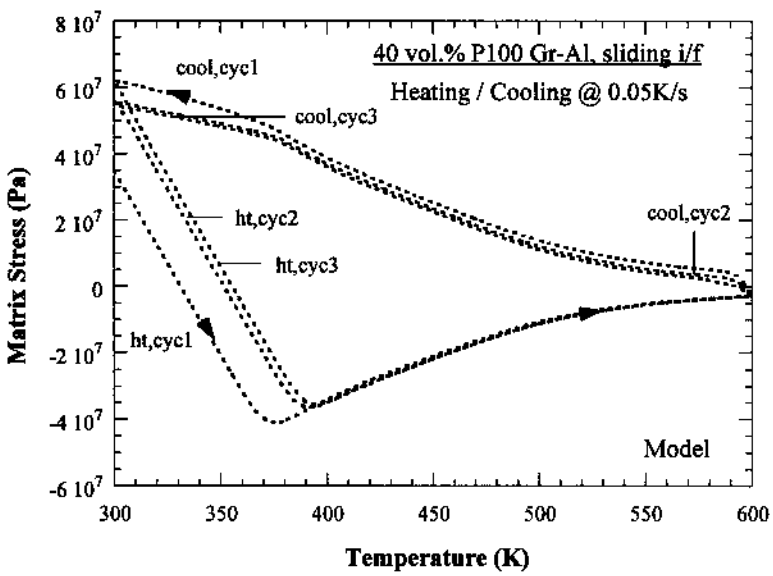

Fig. 11. Computed variation of the axial matrix stress σ_m during three thermal cycles between 300 and 600 K. The initial matrix stress σ_{m_0} is 35 MPa (1st cycle = solid arrows; 2nd cycle = line arrows; 3rd cycle = open arrows).

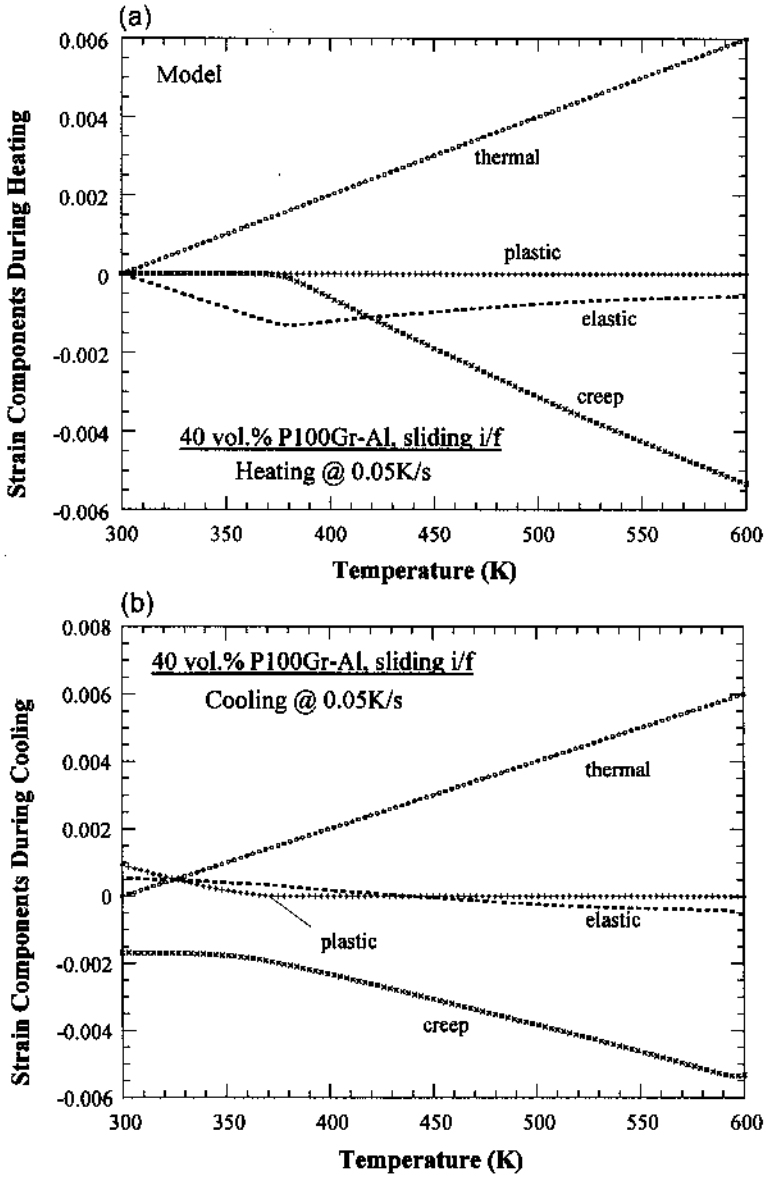

Fig. 12. The variation of thermal, elastic, plastic and total creep strain components during the (a) heating and (b) cooling segments of the first cycle between 300 and 600 K at a rate of 0.05 K/s.

during thermal cycling. For ease of interpretation, the following discussion is based on the first cycle only. Figure 11 plots the axial matrix stress as a function of temperature. Starting from an initial value of 35 MPa, σ_{m_0} gets completely relieved by about 340 K during the first heating excursion, following which a compressive σ_m is induced in the matrix. With progressive heating, this compressive stress builds up, and around 380 K, the operation of creep mechanisms begins stress relief. The knee observed in Fig. 10 is coincidental with the start of this stress relief. At the end of the heating half-cycle (at 600 K), only a small axial compressive stress is left in the matrix. During cooling, the compressive stress is quickly relieved, and a tensile stress builds up throughout the rest of the temperature excursion, ending with a larger induced tensile stress at 300 K (62 MPa) than that present at the beginning of the cycle (35 MPa). This is due to work hardening of the matrix during the latter stages of cooling (and the commensurate increase in yield strength from 58 to 62 MPa), as discussed below.

Figures 12(a) and (b) show the individual matrix strain components during the heating and cooling segments of the first thermal cycle, respectively. The thermal strain increases during heating, and decreases during cooling. The variation of elastic strain is identical to that of the matrix stress σ_m, to

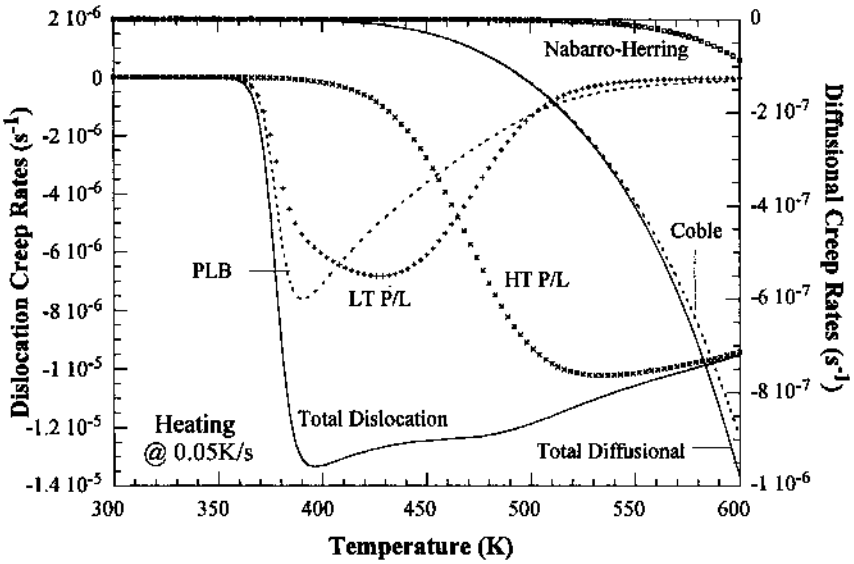

Fig. 13. The variation of the instantaneous strain rates due to different dislocation and diffusional creep mechanisms during the heating segment of the first cycle between 300 and 600 K at 0.05 K/s. The mechanisms addressed include power-law breakdown (PLB), low-temperature or dislocation core diffusion controlled power-law (LT P/L), high temperature or volume diffusion controlled power-law (HT P/L), Coble and Nabarro-Herring creep.

which it is proportional. No plastic strain is induced in the matrix during heating. However, a tensile plastic strain is induced in the matrix during the latter stages of cooling (starting at about 370 K), when the matrix yield strength is exceeded. This leads to work hardening, thereby allowing the final matrix stress to become larger than the initial yield strength. Significant creep strains are induced in the matrix during both heating and cooling above about 380 K, where the matrix creeps in compression during heating, and in tension during cooling. The net permanent strain observed at the end of one thermal cycle in Fig. 10 is compressive since the sum of the magnitudes of the tensile creep and

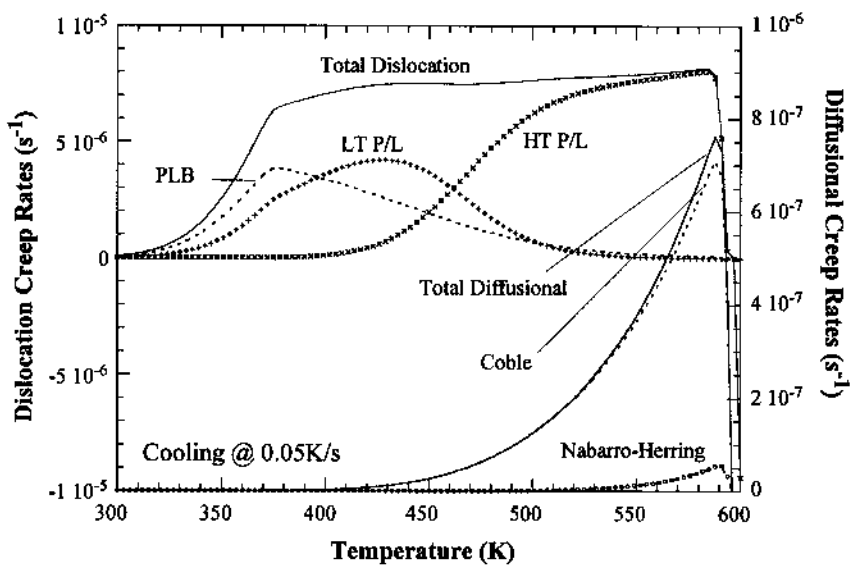

Fig. 14. The variation of the instantaneous strain rates due to different dislocation creep and diffusional creep mechanisms during the cooling segment of the first cycle between 300 and 600 K at 0.05 K/s.

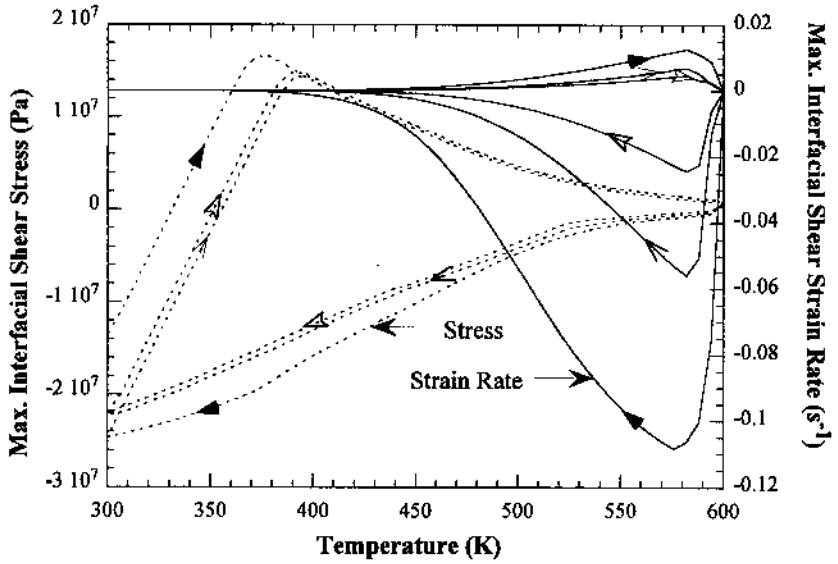

Fig. 15. The variation of the maximum interfacial shear stress, $\tau_i(z = l_0/2)$, and the maximum interfacial shear strain rate, $\dot{\gamma}_i(z = l_0/2)$ during cycling of the composite between 300 and 600 K at 0.05 K/s (1st cycle = solid arrows; 2nd cycle = line arrows; 3rd cycle = open arrows).

plastic strains during cooling is smaller than the compressive creep strain induced during heating.

Figures 13 and 14 show the instantaneous matrix creep strain rates during the heating and cooling segments of the first cycle, respectively. It is apparent that different dislocation creep mechanisms are predominant in different temperature regimes. During heating, creep strains become significant only above ~370°C, whereas during cooling, they are appreciable till lower temperatures. This is because higher matrix stresses exist at the low temperatures during cooling. As expected based on deformation mechanism maps for Al [31], power-law breakdown creep dominates at the lowest temperature (up to ~400 K), dislocation core diffusion controlled power-law creep (low temperature power-law creep) is the dominant mechanism in the intermediate temperature range (~400–460 K), whereas

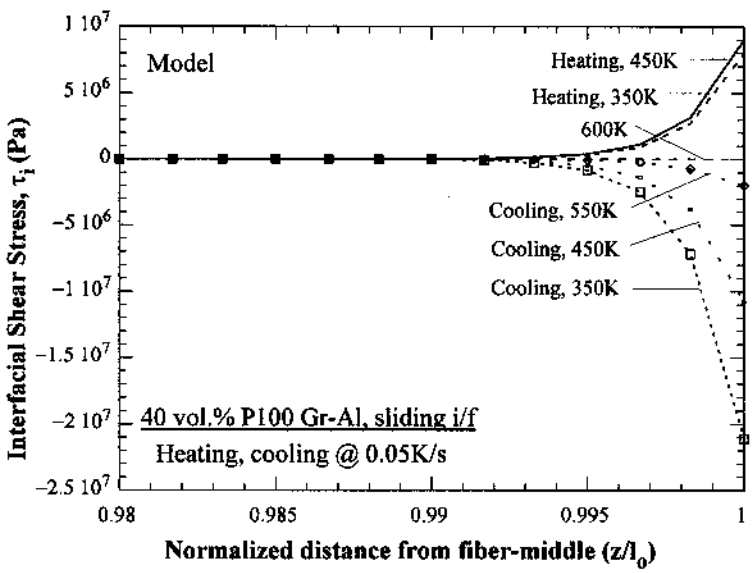

Fig. 16. Computed variation of the interfacial shear stress τ_i along the fiber length close to the fiber-end at different stages of heating and cooling during the first cycle between 300 and 600 K at 0.05 K/s.

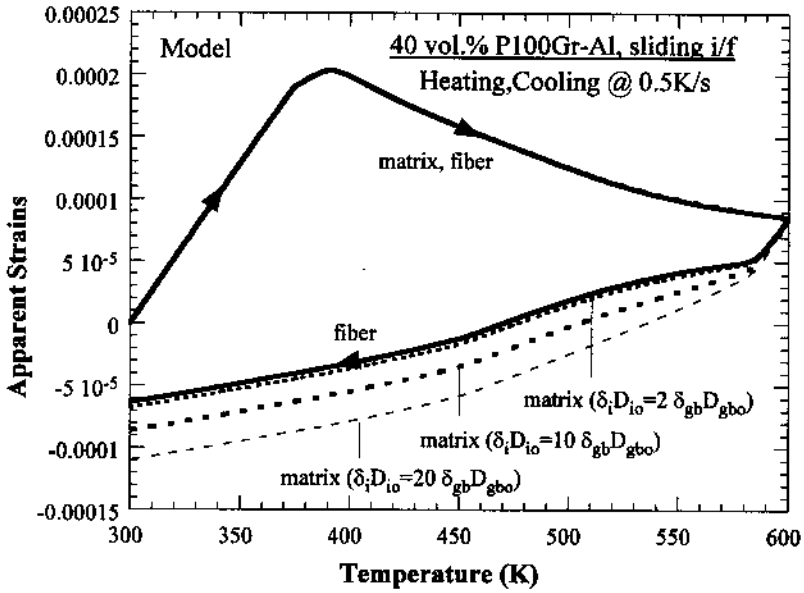

Fig. 17. Computed axial strain response of the composite for one cycle between 300 and 600 K at 0.05 K/s for different values of $\delta_i D_{i_0}$, illustrating the influence of interfacial sliding kinetics.

volume diffusion controlled power-law creep dominates above about 460 K. Thus, the use of unified creep laws is imperative for proper simulation of thermal cycling strains. Figures 13 and 14 also show that for the present thermal cycling conditions and the assumed matrix grain size (25 μm), the diffusional creep rates are much smaller than the dislocation creep rates, with Coble creep being the predominant diffusional creep mechanism.

Figure 15 shows the variation of the maximum interfacial shear stress, $\tau_i(z = l_0/2)$, and the maximum interfacial shear strain rate, $\dot{\gamma}_i(z = l_0/2)$, during three thermal cycles. Commensurate with expansion of the matrix relative to the fiber during

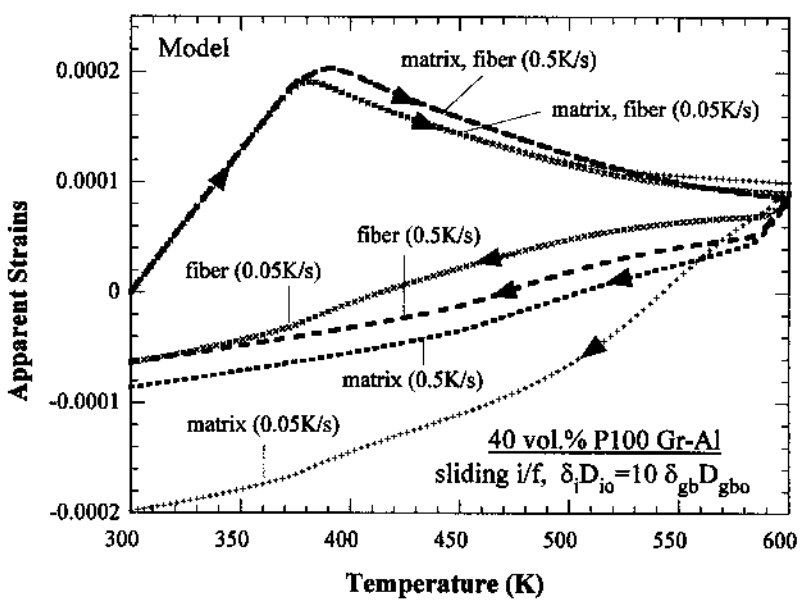

Fig. 18. Computed axial strain response of the composite during one cycle between 300 and 600 K for different values of heating/cooling rates, showing that a slower cycling rate results in a greater divergence between fiber and matrix strains.

the first heating excursion, τ_i, which is negative at the start of cycling, gets relieved around 340 K, and becomes positive thereafter. Beyond 380 K, the continued build-up of τ_i is balanced by partial relief thereof due to matrix creep. During cooling, the matrix contracts relative to the fiber, and τ_i becomes progressively more negative. The interfacial shear strain rate becomes significant only at temperatures above ~380 K and increases with increasing temperatures, but is counteracted by the relief of τ_i at high temperatures. During cooling, the contraction of the matrix relative to the fiber allows τ_i to build up, and this, in conjunction with the high temperatures, results in large interfacial sliding rates. As the temperature drops, however, the magnitude of $\dot{\gamma}_i$ decreases rapidly, despite continued increase in the magnitude of τ_i. During subsequent cycles, the magnitude of τ_i^{max} at the higher temperatures is smaller during both heating and cooling, and therefore, the maximum interfacial shear strain rate also becomes smaller. This results in progressively less interfacial sliding during the second and third cycles.

Figure 16 shows the distribution of the interfacial shear stress τ_i near the fiber-ends at various temperatures during the heating and cooling segments of the first cycle. The abscissa z/l_0 represents the distance along the axial direction from the fiber-middle, normalized by the nominal sample length. It is clear that τ_i (and by hence $\dot{\gamma}_i$) are non-zero only very close to the fiber-ends for the given sample and fiber dimensions. Thus interfacial sliding is confined to within approximately 1% of the length of the sample from each end. Over this length, τ_i starts out being negative at 300 K, switches sign around 330 K and becomes increasingly positive up to 370 K, and then decreases as the temperature rises to 450 K because of creep effects, eventually getting completely relieved at 600 K. During cooling, τ_i becomes progressively more negative. $\dot{\gamma}_i$ follows the same trend as τ_i, except that at 375 K the thermal activation is too small to result in any appreciable interfacial sliding. These trends are consistent with those observed in Fig. 10 for τ_i^{max} and $\dot{\gamma}_i^{max}$ (i.e. τ_i and $\dot{\gamma}_i$ at $z/l_0 = 1$). It should be noted that in general, τ_i and $\dot{\gamma}_i$ are positive when the matrix undergoes longitudinal expansion relative to the fiber, whereas they are negative when the matrix undergoes contraction relative to the fiber.

The impact of the kinetics of interfacial sliding is investigated in Fig. 17, which plots the matrix and fiber strain responses during the first cycle for various values of the parameter $\delta_i D_{i_0}$ [equation (2)]. It is observed that for a heating/cooling rate of 0.5 K/s, there is little interfacial strain during the heating segment. During cooling, however, substantial interfacial sliding occurs, with the matrix shrinking more relative to the fibers for greater values of $\delta_i D_{i_0}$, as expected. Interestingly, there is little impact of interfacial sliding kinetics on the fiber length during thermal cycling, the effect being confined predominantly to the matrix length. This is because faster interfacial sliding kinetics allow greater alleviation of the matrix-constraint by accommodating more creep/plastic deformation, but have little dimensional effect on the fibers which only deform elastically.

Figure 18 shows the effect of heating/cooling rates on the strain response during the first thermal cycle for $\delta_i D_{i_0} = 10\delta_{gb} D_{gb_0}$. The rate effect is observed to be significant. The divergence between the matrix and fiber strains, and therefore the extent of fiber protrusion from the matrix at the end of the cycle, is observed to increase with decreasing heating/cooling rates. This is because of larger cumulative interfacial shear strains at the slower heating/cooling rates. Also of note is the observation that at the end of the heating segment, the matrix length is greater than that of the fiber, whereas at the end of the cycle, the matrix is shorter. This is because the matrix expands more than the fiber during heating, and contracts more than the fiber during cooling, this differential expansion/contraction being accommodated by interfacial creep. Since the cumulative interfacial shear strain induced during cooling is greater than that induced during heating, the matrix ends up being shorter than the fiber at the end of the cycle despite being longer at the end of the heating segment.

4. DISCUSSION

Comparing Figs 2 and 3 with Figs 8 and 10, respectively, it is apparent that although the analytical results are not in exact quantitative agreement with experiments, they capture all the essential features of the experimental strain response, including the extrusion/intrusion of fiber-ends relative to the matrix at the end of cycling, as observed in Figs 4 and 5. In fact, the noted deviation is not unreasonable considering (i) the analytical results are based on a pure Al matrix instead of Al 6061 in the experiments; (ii) the interfacial creep data were estimates; (iii) the matrix was assumed to creep in steady state only; and (iv) the available creep data for various mechanisms in pure Al, although considered to be the most comprehensive available, are not necessarily very accurate since they are often estimated from significantly divergent experimental results [31].

Both the experimental and the analytical results presented above indicate that the composite strain response is strongly rate dependent, an effect that has often not been explicitly recognized in the literature (e.g. Refs [3–8, 36–38]). As shown above, this rate dependence arises from two separate phenomena: (i) matrix creep and (ii) diffusionally accommodated interfacial sliding.

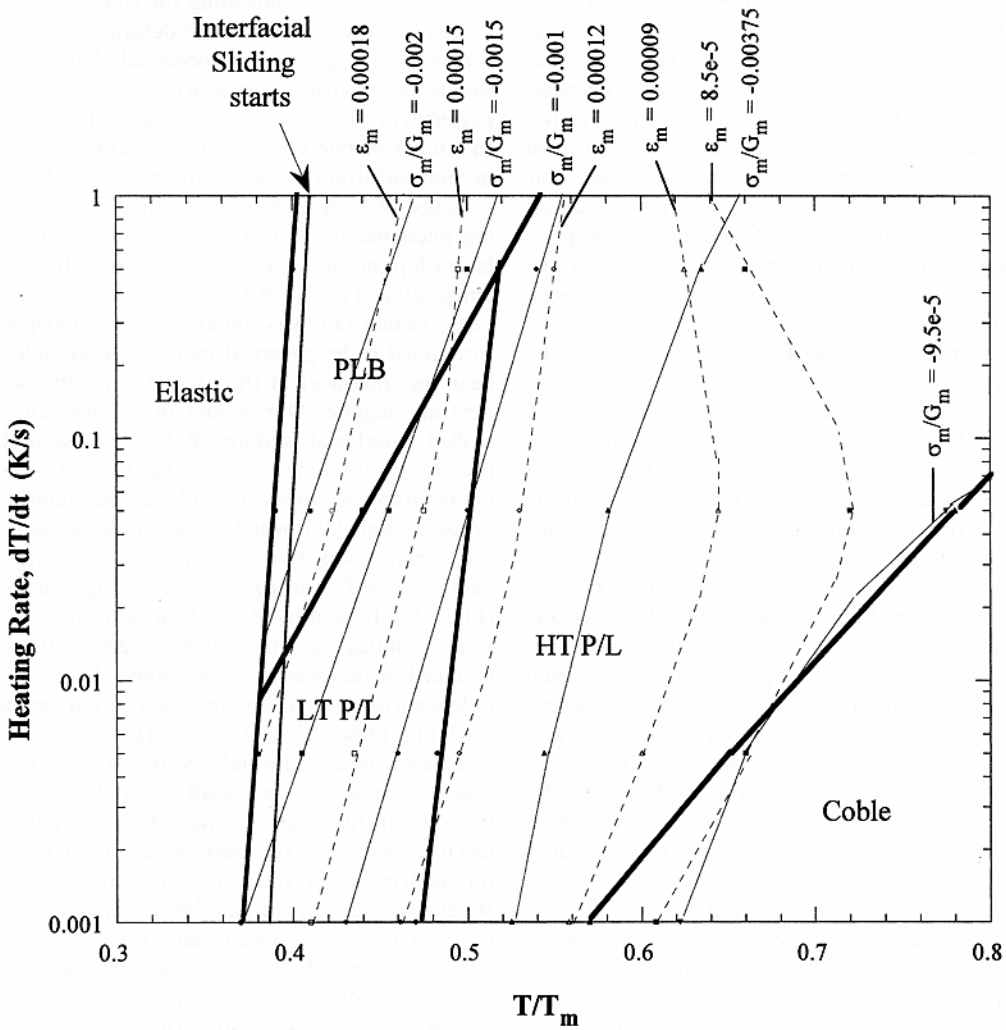

Fig. 19. A transient deformation mechanism map for the first heating segment of a graphite–Al composite with $\sigma_{m_0} = 35$ MPa, showing the matrix deformation mechanisms operative in different heating rate–homologous temperature regimes. Also shown are contours of constant total matrix strain and modulus-compensated stress. In addition to identifying the dominant matrix deformation mechanism, the plot can be utilized to predict the overall strain response and instantaneous matrix stress during heating of the composite at any given rate.

Although many of the characteristics of the thermal strain response of composites such as strain hysteresis and the knee in the heating curve are explicable without consideration of rate-dependent plasticity (e.g. Ref. [36]), other features, such as the residual permanent strain, and the intrusion/protrusion of fiber-ends relative to the matrix at the end of cycling are more difficult to rationalize solely on the basis of rate-independent plasticity. In the *slow* cycling regime, where the present work is applicable, stress relief mechanisms start operating early on during the heating segment, never allowing the matrix stress to exceed the temperature-dependent yield strength. This precludes matrix yielding during heating, which is essential for rationalizing the observed knee if rate effects are ignored [36]. Furthermore, in the absence of matrix creep, the heating rate dependence of the temperature at which the knee occurs (as evident from a comparison of Figs 2 and 3) is not explicable.

Another manifestation of rate-dependent plasticity is the residual permanent strain that is frequently observed at the end of one cycle. As noted earlier, during initial cooling from the fabrication temperature, the matrix undergoes plastic deformation (and hence work hardening), allowing the matrix yield strength (and the new matrix stress) to increase beyond the yield strength of the annealed matrix. During storage in the as-fabricated state, some stress relaxation usually occurs (such stress relaxation has been clearly noted for SiC_w/Al composites at room temperature via neutron diffraction studies [39]), allowing the matrix stress to drop well below the yield strength. As shown above, such a

decrease in the initial matrix stress (σ_{m_0}) from 58 to 35 MPa leads to a significant compressive permanent strain at the end of the cycle, similar to that observed experimentally. This is because a decrease in σ_{m_0} places the matrix in compression earlier during the heating segment, allowing it to creep in compression over a wider temperature range. This relationship between the extent of stress relaxation prior to cycling and the magnitude of the compressive permanent strain observed at the end of the cycle ($\Delta\varepsilon_{m_p}$) may be the reason why $\Delta\varepsilon_{m_0}$ has been variously found to be zero, small or significant in different experiments (see Refs [2, 6–11, 38] and the present study).

Even when the effect of matrix creep has been recognized (e.g. Refs [2, 9–11]), transitions in the matrix creep mechanism during thermal cycling (demonstrated in Figs 13 and 14), and their effects on the overall thermal strain response, have not been considered. The present computations show that plots of the instantaneous creep strain rates vs temperature (e.g. Figs 13 and 14) display a strong dependence on the rate of temperature excursion. Thus the temperature range within which each creep mechanism predominates is strongly dependent on the heating or cooling rate. This rate and temperature dependence of the operative creep mechanism may be summarized in the form of a deformation mechanism map such as that shown in Fig. 19 (plotted for the heating segment of the first thermal cycle), where the different matrix deformation mechanism fields are identified as functions of the heating rate (dT/dt) and the homologous temperature (T/T_m). Also shown in the map are contours of constant modulus compensated matrix stress (σ_m/G_m) and total matrix strain (ε_m). Although the map is based on steady state matrix creep mechanisms, it represents a *transient* deformation mechanism map since σ_m/G_m and the matrix strain rate $\dot{\varepsilon}_m$ vary continuously during a temperature excursion. Such transient deformation mechanism maps may be utilized to estimate the matrix stress and strain (and hence the composite strain) states at any instant during a thermal excursion for any given heating/cooling rate. It should be noted that the details of such maps are strongly dependent upon the thermal strain history of the material (i.e. initial matrix strain and stress states at the start of each thermal excursion), and therefore must be constructed separately for the heating and cooling segments of different cycles. Nevertheless, such maps provide a useful tool in offering insight into the different deformation mechanisms prevalent in a composite at different stages during a temperature excursion.

It was observed from Fig. 15 that interfacial sliding via creep mechanisms becomes prevalent above ~ 380 K for a heating rate of 0.05 K/s. Computations showed that this temperature is relatively insensitive to the heating/cooling rate. Accordingly, a line indicating the start of interfacial sliding has been added to the deformation mechanism map in Fig. 19. It is observed that interfacial sliding is prevalent over nearly the entire range of parameters where matrix creep mechanisms operate. In studies of rate effects at metal–ceramic interfaces in film–substrate systems, Jobin *et al.* [40] found evidence of a strongly rate sensitive interfacial sliding phenomenon with a linear stress–strain rate relationship in the low strain rate ($\dot{\varepsilon} \lesssim 10^{-4}$/s)/high temperature ($T/T_m \gtrsim 0.3$) regime, whereas the interfacial sliding rate was found to be rate-independent (presumed to be governed by dislocation glide at or near the interface) in the high strain rate/low temperature regime. Our model of diffusionally controlled interfacial sliding (Refs [26, 28] and the present study) based on the behavior at elevated temperatures is consistent with the mechanism proposed in Ref. [40], which is also in agreement with our observation that the interfacial sliding rate below $\sim 0.38 T_m$ during thermal cycling is negligible (Fig. 19). It is possible that in addition to diffusional sliding at the higher temperatures, as assumed in the present model, some sliding by rate-independent mechanisms may also occur below the start line indicated in Fig. 19. However, the total interfacial shear strain induced due to such a mechanism is likely to be small compared with that induced at the higher temperature by diffusional mechanisms, since the heating rate (and therefore, the matrix strain rates involved) are very small. Whereas faster heating rates may increase the likelihood of perceptible interfacial strains by rate-independent sliding, they also increase the likelihood of frictional sliding following interfacial debonding (e.g. Refs [9, 12]), suggesting that the low-temperature sliding mechanism proposed by Jobin *et al.* may not necessarily be important in composites.

5. CONCLUSIONS

A simple micro-mechanical model has been developed in order to provide insight into the roles of interfacial and matrix creep during thermal cycling of continuous fiber composites. Unlike previous efforts, the present model incorporates the effects of interfacial sliding and matrix creep mechanism transitions at various stages during thermal cycling. The fiber and the matrix are modeled as thermo-elastic and thermo-elasto-plastic-creeping solids, respectively, whereas the interface was assumed to slide via diffusion-controlled diffusional creep with a threshold stress related to the normal stress acting on the interface.

The results of the model are in good qualitative agreement with experimental dilatometry results based on a continuous graphite fiber reinforced aluminum composite. The model could successfully rationalize all the important features of the experimental strain response, including the incompatibil-

ities in the longitudinal matrix and fiber strains, which is reflected by either intrusion or protrusion of the fiber-ends relative to the matrix at the end of a thermal cycle.

The strain response during thermal cycling was found to be strongly rate dependent, suggesting the important roles of both matrix and interfacial creep. Interfacial creep was found to be confined only to a very small region near the fiber-ends where shear stresses are significant, but under appropriate conditions, resulted in appreciable differential strain between the matrix and fiber. The extent of differential strain induced in each cycle, however, decreased with progressive cycling. Matrix creep, which depends strongly on the instantaneous stress and temperature, was found to undergo several mechanistic transitions at different stages of thermal cycling, making the use of unified creep laws imperative for realistic simulations of the composite strain response. Based on the results of the analysis, a *transient deformation mechanism map for thermal cycling*, that plots the heating/cooling rate (dT/dt) against the homologous temperature (T/T_m), has been constructed. The plot also includes contours of constant matrix stress and strain, and can be utilized to predict (i) the matrix strain and stress states, and (ii) the dominant matrix deformation mechanism, at any instant during a thermal excursion. The field for interfacial sliding, which overlaps nearly the entire range of conditions over which matrix creep is prevalent, is also indicated in the map.

Acknowledgements—This work was supported by the National Science Foundation, Division of Materials Research, under contract number DMR-9423668 with Dr B. A. MacDonald as program monitor. The author gratefully acknowledges the contributions of J. V. Funn, A. D. Wiest, M. Esmele, R. Nagarajan and Y. Farsaris to various aspects of the experimental and analytical work.

REFERENCES

1. Kreider, K. G. and Patarini, V. M., *Metall. Trans.*, 1970, **1**, 3431.
2. Garmong, G., *Metall. Trans.*, 1974, **5**, 2191.
3. Wakashima, K., Otsuka, M. and Umekawa, S., *J. Compos. Mater.*, 1974, **8**, 391.
4. Wolff, E. G., in *Proc. Eighth Int. Thermal Expansion Symp.*, ed. T. A. Hahn. American Institute of Physics, New York, 1981.
5. Kural, M. H. and Min, B. K., *J. Compos. Mater.*, 1984, **18**, 519.
6. Dries, G. A. and Tompkins, S. S., NASA TP #2402, NASA-Langley Research Center, Hampton, VA, 1985.
7. Dries, G. A. and Tompkins, S. S., NASA TP #2612, NASA-Langley Research Center, Hampton, VA, 1986.
8. Dries, G. A. and Tompkins, S. S., NASA TP #2701, NASA-Langley Research Center, Hampton, VA, 1987.
9. Mitra, S., Dutta, I. and Hansen, R. C., *J. Mater. Sci.*, 1991, **26**, 6223.
10. Dutta, I., Mitra, S. and Wiest, A. D., in *Residual Stresses in Composites—Measurement, Modeling and Effects on Thermo-Mechanical Behavior*, ed. E. V. Barrera and I. Dutta. TMS–AIME, Warrendale, PA, 1993, p. 273.
11. Yoda, S., Kurihara, N., Wakashima, K. and Umekawa, S., *Metall. Trans.*, 1978, **9A**, 234.
12. Cox, B. N., *Acta metall. mater.*, 1990, **38**, 2411.
13. Hoffman, C. A., *J. Engng Mater.*, 1973, **95**, 805.
14. Garmong, G., *Metall. Trans.*, 1974, **5**, 2183.
15. Tyson, W. R., *Metall. Trans.*, 1975, **6A**, 1674.
16. Zhang, H., Anderson, P. M. and Daehn, G. S., *Metall. Trans. A*, 1994, **25A**, 415.
17. Furness, J. A. G. and Clyne, T. W., *Mater. Sci. Engng*, 1991, **A141**, 199.
18. Goto, S. and Mclean, M., *Acta metall. mater.*, 1991, **39**, 153.
19. Dlouhy, A., Merk, N. and Eggeler, G., *Acta metall. mater.*, 1993, **41**, 3245.
20. Dlouhy, A., Eggeler, G. and Merk, N., *Acta metall. mater.*, 1995, **43**, 535.
21. Kelly, A. and Street, K. N., *Proc. R. Soc. Lond. A*, 1972, **328**, 2073.
22. Bullock, E., Mclean, M. and Miles, D. E., *Acta metall.*, 1977, **25**, 333.
23. Kim, K. T. and McMeeking, R. M., *Mech. Mater.*, 1995, **20**, 153.
24. Nimmagadda, P. B. R. and Sofronis, P., *Mech. Mater.*, 1996, **23**, 1.
25. Sofronis, P. and McMeeking, R. M., *Mech. Mater.*, 1992, **18**, 55.
26. Funn, J. V. and Dutta, I., *Acta mater.*, 1999, **47**, 149.
27. Raj, R. and Ashby, M. F., *Metall. Trans.*, 1971, **2**, 1113.
28. Nagarajan, R., Dutta, I., Funn, J. V. and Esmele, M., *Mater. Sci. Engng*, 1999, **A259**, 237.
29. Dutta, I., *Key Engng Mater.*, 1995, **104–107**, 673.
30. Shen, Y. L. and Suresh, S., *Acta mater.*, 1996, **44**, 1337.
31. Frost, H. J. and Ashby, M. F., *Deformation Mechanism Maps—Plasticity and Creep of Metals and Ceramics*. Pergamon Press, Oxford, 1982.
32. Garofalo, F., *Trans. metall. Soc. A.I.M.E.*, 1963, **227**, 351.
33. Dresselhaus, M. S., Dresselhaus, G., Sugihara, K., Spain, I. L. and Goldberg, H. A., *Graphite Fibers and Filaments*. Springer-Verlag, Berlin, 1988.
34. *Metals Handbook: Properties and Selection: Nonferrous Alloys and Special Purpose Materials*, 10th edn. ASM International, Metals Park, OH, 1990.
35. Tsai, S. D., Mahulikar, D., Marcus, H. L., Noyan, I. C. and Cohen, J. B., *Mater. Sci. Engng*, 1981, **47**, 145.
36. Rabinovitch, M., Stohr, J. F., Khan, T. and Bibring, H., in *Handbook of Composites, Vol. 4—Fabrication of Composites*, ed. A. Kelly and S. T. Mileiko. Elsevier, Amsterdam, 1983, p. 295.
37. Yamada, S. and Towata, S., *J. Japan Inst. Metals*, 1985, **49**, 376.
38. Masutti, D., Lentz, J. P. and Delannay, F., *J. Mater. Sci. Lett.*, 1990, **9**, 340.
39. Withers, P. J., Jensen, D. J., Lilholt, H. and Stobbs, W. M., in *Proc. ICCM VI/ECCM2*, ed. F. C. Matthews, N. C. R. Buskell, J. M. Hodgkinson and J. Morton. Elsevier, Amsterdam, 1987, pp. 2.255–2.264.
40. Jobin, V. C., Raj, R. and Phoenix, S. L., *Acta metall. mater.*, 1992, **40**, 2269.

APPENDIX

Expressions for matrix and fiber strain components

The fiber undergoes thermal and elastic defor-

mation only, the total axial fiber strain being given by

$$\varepsilon_f = (\varepsilon_f^{th} + \varepsilon_f^{el}) \tag{A1}$$

where

$$\varepsilon_f^{th} = \int_{T_2}^{T_1} \alpha_f \, dT \quad \text{and} \quad \varepsilon_f^{el} = \frac{\sigma_f}{E_f}$$

and T_1 and T_2 are the lower and upper limits of temperature during a thermal excursion, α_f is the thermal expansion coefficient of the fiber and E_f is the Young's modulus of the fiber along the axial direction.

The matrix undergoes thermal, elastic, plastic and creep deformation. The total axial matrix strain is given by

$$\varepsilon_m = (\varepsilon_m^{th} + \varepsilon_m^{el} + \varepsilon_m^{pl} + \varepsilon_m^{cr}) \tag{A2}$$

where superscripts th, el, pl and cr refer to thermal, elastic, plastic and creep deformation, respectively. The thermal and elastic axial strains of the matrix are

$$\varepsilon_m^{th} = \int_{T_1}^{T_2} \alpha_m \, dT \quad \text{and} \quad \varepsilon_m^{el} = \frac{\sigma_m}{E_m}$$

where α_m is the linear thermal expansion coefficient of the matrix and E_m is the Young's modulus of the matrix in the axial direction. The plastic strain can be derived from Ludwik's relation and is given by

$$\varepsilon_m^{pl} = \left[\frac{(\sigma_m - \sigma_m^{ys})}{K_1}\right]^{1/n_1} \tag{A3}$$

where σ_m^{ys} is the matrix yield stress, and K_1 and n_1 are the work hardening coefficient and exponent, respectively.

For the creep strain, both the dislocation and diffusional contributions have been taken into consideration. The total steady state creep strain may be written as

$$\varepsilon_m^{cr} = \dot{\varepsilon}_m^{disl} t + \dot{\varepsilon}_m^{diff} t \tag{A4}$$

where superscripts diff and disl represent the diffusional and dislocation creep components, respectively.

The dislocation creep strain rate may be written as [31,32]

$$\dot{\varepsilon}_m^{disl} = A_{disl}\left[\sinh\left(\frac{\alpha'}{\sqrt{3}G_m}\sigma_m\right)\right]^n \tag{A5}$$

where

$$A_{disl} = \left(\frac{\sqrt{3}}{\alpha'}\right)\frac{AG_m b}{kT} D_{eff}^{disl}$$

and

$$D_{eff}^{disl} = \left[D_L + \left(\frac{10}{3b^2 G_m^2}\right)\sigma_m^2 a_p D_p\right].$$

n is the stress exponent for dislocation creep, α' is the power-law breakdown parameter, G_m is the shear modulus, A is the creep constant, b is the Burger's vector, a_p is the cross sectional area of the dislocation core, D_p is the pipe diffusivity and T is the absolute temperature.

The diffusional creep rate can be written as [31]

$$\dot{\varepsilon}_m^{diff} = A_{diff}\sigma_m \tag{A6}$$

where

$$A_{diff} = \frac{14\Omega}{kTd^2}\left[D_L + \left(\frac{\pi}{d}\right)\delta_{gb} D_{gb}\right].$$

Ω is the atomic volume, d is the matrix grain size, δ_{gb} is the effective thickness of the grain boundary, D_{gb} is the grain boundary diffusivity and D_L is the volume diffusivity.